

# Power spectrum of the cosmic infrared background at 60 and 100 $\mu\text{m}$ with IRAS

M.-A. Miville-Deschênes<sup>1</sup>, G. Lagache<sup>2</sup>, and J.-L. Puget<sup>2</sup>

<sup>1</sup> Laboratoire de radioastronomie, École Normale Supérieure, 24 rue Lhomond, 75005, Paris, France

<sup>2</sup> Institut d'Astrophysique Spatiale, Université Paris-Sud, Bât. 121, 91405, Orsay, France.

October 26, 2018

**Abstract.** Based on a power spectrum analysis of the IRAS ISSA maps, we present the first detection of the Cosmic far-Infrared Background (CIB) fluctuations at 60 and 100  $\mu\text{m}$ . The power spectrum of 12 low cirrus emission regions is characterized by a power excess at spatial frequencies higher than  $k \sim 0.02 \text{ arcmin}^{-1}$ . Most of this excess is due to noise and to nearby point sources with a flux stronger than 1 Jy. But we show that when these contributions are carefully removed, there is still a power excess that is the signature of the CIB fluctuations. The power spectrum of the CIB at 60 and 100  $\mu\text{m}$  is compatible with a Poissonian distribution, at spatial frequencies between 0.025 and 0.2  $\text{arcmin}^{-1}$ . The fluctuation level is  $\sim 1.6 \times 10^3 \text{ Jy}^2/\text{sr}$  and  $\sim 5.8 \times 10^3 \text{ Jy}^2/\text{sr}$  at 60 and 100  $\mu\text{m}$  respectively. The levels of the fluctuations are used in a larger framework, with other observational data, to constrain the evolution of IR galaxies (Lagache et al. 2002). The detections reported here, coupled with the level of the fluctuations at 170  $\mu\text{m}$ , give strong constraints on the evolution of the IR luminosity function. The combined results at 60, 100 and 170  $\mu\text{m}$  for the CIB and its fluctuations allows, on the CIB at 60  $\mu\text{m}$ , to put a firm upper limit of 0.27 MJy/sr and to give an estimate of 0.18 MJy/sr.

**Key words.** cosmology: diffuse radiation, infrared: ISM, infrared: general

## 1. Introduction

The Cosmic Far-Infrared Background (CIB) was detected by Puget et al. (1996), exploiting COBE-FIRAS data, and has now been firmly established over a range of wavelengths (e.g. Dwek et al. (1998); Gispert et al. (2000); Hauser & Dwek (2001)). The intensity is quite high with respect to predictions based on evolutionary models of star formation in galaxy populations inferred from optical data. Source counts obtained with SCUBA at 850  $\mu\text{m}$  and ISO at 170 and 15  $\mu\text{m}$  have partly resolved the CIB and shown a strong cosmological evolution. In the future, far-IR and sub-millimeter telescopes from ground and space will perform deep surveys over small areas, aimed at resolving a substantial fraction of the CIB and to shed light on the number density, luminosity and spectral evolution of the infrared galaxy populations. However, investigation of the clustering of these populations requires surveys over much larger areas. One way to tackle the limitation on the number of detected galaxies per field is to search for CIB fluctuations. So far, CIB fluctuations has only been observed at 170  $\mu\text{m}$  in the FIRBACK fields (Lagache & Puget 2000) and at 90 and 170  $\mu\text{m}$  in the

Lockman hole (Matsuhara et al. 2000) surveys. These detections were probably dominated by the Poissonian contribution. By analyzing larger FIRBACK fields, power spectra seem to reveal correlated fluctuations, well above the cirrus contribution (Puget & Lagache 2002). These results are currently under further investigation. Above 170  $\mu\text{m}$ , only SCUBA observations might currently be able to give information on the fluctuations. However, no significant CIB correlations have been detected in the SCUBA maps (Peacock et al. 2000). The CIB anisotropies are mainly contributed by moderate to high redshift star-forming galaxies, whose clustering properties and evolutionary histories are currently unknown. Since the clustering strength depends on the bias at the relevant redshift, observing the CIB correlated fluctuations will provide valuable informations on bulge and elliptical formation, as well as potentially QSOs, thereby providing clues on the physical relations between dark matter and starburst galaxies.

In this paper we present the results of a power spectrum analysis of the IRAS 60 and 100  $\mu\text{m}$  emission of 12 regions in the sky with very low interstellar emission. All these regions are characterized by an excess of power at high spatial frequencies with respect to the interstellar emission. We will show that this excess is not of instrumental origin

and may be attributed to the CIB. The discovery of the CIB fluctuations at 60 and 100  $\mu\text{m}$  could give constraints on the number counts below the IRAS point source detection limit. However, instead of extrapolating the number counts at 60 and 100  $\mu\text{m}$  using the level of the fluctuations, which is of limited cosmological interest, we prefer to use the two detections in a more general framework of the modelisation of the IR galaxy evolution that combines all existing number counts, redshift distributions, and observations of the CIB and its fluctuations, in the whole IR and submm range Lagache et al. (2002).

The paper is organized as follow. After a presentation (§ 2) of the data used for this analysis we describe in § 3 the power spectrum at 60 and 100  $\mu\text{m}$  of the 12 fields selected. In § 4 we present the method used to separate the Galactic and extra-Galactic contributions to the power spectrum and we discuss our results in § 5.

## 2. Data - the ISSA maps

### 2.1. The IRAS Sky Survey Atlas

The IRAS mission was originally designed to measure point sources but it also provided spectacular images of the Galactic dust diffuse emission. These images, constituted of  $500 \times 500$  pixels with a pixel size of  $1.5'$  (i.e. the size of the field is  $12.5^\circ \times 12.5^\circ$ ), are gathered in the IRAS Sky Survey Atlas (ISSA). Each ISSA map is the result of the combination of up to three individual maps (named for HCON Hours CONfirmation). The HCON images were constructed from different observations of the same region separated by several months. The angular resolution of the 60 and 100  $\mu\text{m}$  band images are respectively  $1.5' \times 4.7'$  and  $3.0' \times 5.0'$ . To study the power spectrum of the CIB emission at 60 and 100  $\mu\text{m}$ , we have worked on 12 ISSA maps with particularly low cirrus emission.

### 2.2. Calibration of the ISSA maps

Special care has been taken to have a consistent diffuse emission calibration through the Atlas. But, as the IRAS mission was designed to provide absolute photometry only for point sources, the ISSA images give only relative photometry and cannot be used to determine the absolute surface brightness for diffuse emission. Based on a comparison with the DIRBE data, it has been shown (Wheelock et al. 1993; Schlegel et al. 1998) that, at large scale ( $> 4$  a few degrees), the amplitude of the fluctuations are overestimated in the ISSA maps by a factor 1.15 at 60  $\mu\text{m}$  and 1.39 at 100  $\mu\text{m}$ . We have thus applied these factors to our maps prior to the analysis.

There is also an uncertainty on the zero level of the ISSA maps, for which the zodiacal emission has been subtracted (Wheelock et al. 1993). This uncertainty is dominated at 60 and 100  $\mu\text{m}$  by an imperfect knowledge of the detector offsets and of the zodiacal emission. As we are looking at fluctuations of the signal, a global additive offset has no impact on the power spectrum. On the other

ISSA	$\alpha_{2000}$	$\delta_{2000}$	l	b
47	4h 1m 24.8s	-49° 51' 41.5"	258.32°	-47.41°
66	23h 2m 53.8s	-49° 43' 50"	338.21°	-59.30°
69	1h 46m 9.0s	-39° 45' 1"	264.42°	-73.02°
71	3h 29m 49.5s	-39° 49' 46"	244.45°	-54.96°
97	1h 34m 18.6s	-29° 44' 39"	230.96°	-80.22°
322	13h 4m 23.3s	29° 43' 55"	76.14°	86.14°
323	13h 50m 16.1s	29° 45' 9"	47.86°	76.81°
348	9h 35m 7.0s	39° 46' 35"	182.59°	47.71°
349	10h 26m 56.1s	39° 44' 41"	180.70°	57.59°
356	16h 29m 42.1s	39° 53' 31"	63.41°	43.50°
375	10h 3m 12.9s	49° 45' 28"	166.14°	50.80°
376	11h 2m 53.8s	49° 43' 50"	158.21°	59.30°

**Table 1.** Central pixel coordinates (ecliptic and Galactic) of the 12 ISSA maps selected for our analysis.

hand, an imperfect zodiacal emission correction applied to the ISSA maps will have an impact on the large scale structure of the maps and then on the power spectrum (for low  $k$  values). To restore appropriately the large scale structure of the selected fields we have compared each ISSA map with the DIRBE data (for which the zodiacal emission correction was better done). The ISSA maps, multiplied by the appropriate gain value (0.87 at 60  $\mu\text{m}$  and 0.72 at 100  $\mu\text{m}$ ) were convolved by the DIRBE beam and then subtracted from the DIRBE data. This offset map is then added to the ISSA map. Note that we do not use the Schlegel et al. (1998) IRAS rescaled maps, constructed in a similar manner, for which it is impossible to recover the associated instrumental noise.

### 2.3. Fields with low cirrus emission

In this paper we present a power spectrum analysis of twelve high latitude fields. These fields were selected on the basis of their low cirrus emission (mean brightness  $\sim 1$  MJy/sr at 100  $\mu\text{m}$ ) but also on their redundancy; we have selected only fields for which each sky position has been observed at least twice in order to be able to estimate the contribution of the noise to the power spectrum. The typical stripping of the ISSA maps is very efficiently removed from the signal power spectrum by the noise estimate procedure using the difference between observations of the different HCON as will be shown in § 3.3 and Fig. 2.

The 60 and 100  $\mu\text{m}$  ISSA maps of the twelve selected fields, gain and offset corrected, are shown in Figs A.2 to A.3 and their central coordinates are gathered in Table 1. Five fields are located in the southern hemisphere, most of them in the neighborhood of the Marano field (Marano et al. 1988), and seven are spread over the northern hemisphere (ISSA map number 376 contains the Lockman Hole).

## 3. Power spectrum of the 60 and 100 $\mu\text{m}$ sky

### 3.1. Power spectrum computation

For a given image, the power spectrum  $P(k)$  is the absolute value of the Fourier Transform (we use the Fast Fourier Transform (FFT) function of IDL) of the image, averaged over constant values of  $k = \sqrt{k_x^2 + k_y^2}$ . To make sure that map boundaries are not contaminating the computed power spectrum, we apodize the image with a cosine function before computing the Fourier Transform. This prevents the introduction of strong discontinuities when the image is periodized in the FFT algorithm (see Appendix A).

The power spectrum of the 100  $\mu\text{m}$  ISSA map of one of our fields is shown in Fig. 1. Since the zodiacal emission has been subtracted in the ISSA maps, there are four main contributions to the power spectrum at these wavelengths: the cirrus emission, point sources, the CIB (resolved and unresolved) and the noise. Therefore, and if the noise and the signal are not correlated, the power spectrum  $P(k)$  can be expressed in the following manner:

$$P(k) = \gamma(k) [P_{\text{dust}}(k) + P_{\text{source}}(k) + P_{\text{cib}}(k)] + N(k) \quad (1)$$

where  $P_{\text{dust}}(k)$ ,  $P_{\text{cib}}(k)$ ,  $P_{\text{source}}(k)$  and  $N(k)$  are respectively the power spectrum of the dust emission, of the CIB, of individually detected point sources and of the noise. The factor  $\gamma(k)$  represents the instrumental function.

### 3.2. Noise power spectrum

One of the main limitation of the component separation to the power spectrum is the estimate of the noise contribution. For ISSA maps, this contribution can be estimated accurately as they are the combination of up to three HCON maps. Indeed the noise power spectrum of the HCON maps, and therefore of the ISSA map, can be estimated by subtracting two HCON maps of the same region. An example of the difference between two HCON maps for a typical low brightness ISSA map is shown in Fig. 1 (top-right). The characteristic stripping of the IRA data is seen in this difference map. The distribution of difference values is symmetric (when there is no strong point sources) and well fitted by a sum of two Gaussian functions (see Fig. 1, bottom-right).

As the distribution of the difference values is the sum of two Gaussian functions with an equivalent width  $\sigma_{\text{di}}$  and assuming that the noise in the IRAS survey is stationary to a good approximation (as tested below), we can conclude that the noise of an individual HCON can also be characterized by an equivalent width:

$$\sigma_{\text{hcon}} = \frac{\sigma_{\text{diff}}}{\sqrt{2}}. \quad (2)$$

Furthermore, the noise of the ISSA map, built from  $n$  HCON maps, is also Gaussian distributed with a width of:

$$\sigma_{\text{issa}} = \frac{\sigma_{\text{hcon}}}{\sqrt{n}}. \quad (3)$$

Therefore, the noise level of the ISSA map is given by:

$$\sigma_{\text{issa}} = \frac{\sigma_{\text{diff}}}{\sqrt{n}\sqrt{2}}. \quad (4)$$

For the example given in Fig. 1, the noise level is  $\sigma_{\text{issa}} = 0.048 \text{ MJy/sr}$ .

In general three HCON maps were averaged but parts of them may be undefined. Therefore, for each ISSA map we looked at the three corresponding HCON maps and built a mask  $n(x, y)$  that gives the number of defined values that were averaged at each positions. Then, the noise map of a given ISSA map is estimated by subtracting two HCON maps and divide the result by  $\sqrt{2}\sqrt{n(x, y)}$ .

The power spectra of the ISSA map and of its noise map are shown in Fig. 1(bottom-left). Both power spectra meet at small scales ( $k \sim 0.2 \text{ pixel}^{-1}$ ) where the signal is noise dominated. The noise map is characterized by a  $\sim k^{-0.8}$  power spectrum. We have investigated the variations of the statistical properties of the noise on ISSA maps where three complete HCONs exists. By looking at the three possible difference maps built from three HCONs, we found that the shape of the power spectrum of the noise is rather constant with time and that the absolute level of the noise varies by less than 15% from one HCON to the other. This is equally true at 60 and 100  $\mu\text{m}$ .

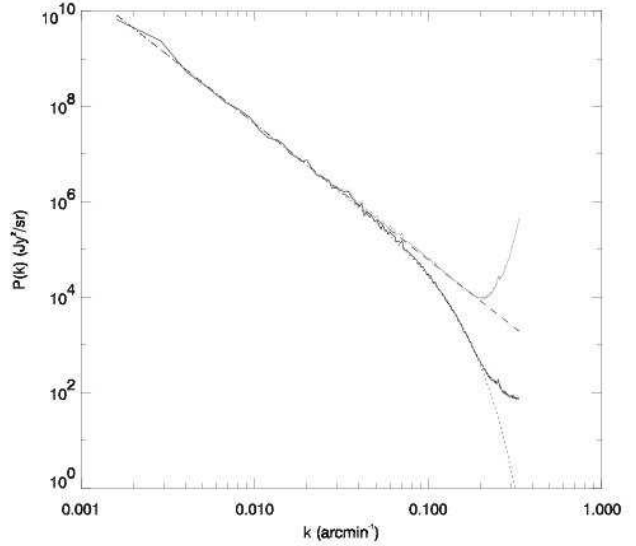


**Fig. 2.** Power spectrum (black solid line) of a typical bright ISSA field with no strong point sources. The cirrus contribution to the power spectrum has been fitted by a power law ( $P(k) \propto k^{-2.86}$  for  $k < 0.015 \text{ arcmin}^{-1}$  - dash line). The dotted line is the cirrus fit multiplied by a Gaussian PSF of  $\sigma = 0.07 \text{ arcmin}^{-1}$ . The grey line is the power spectrum of the ISSA map (black solid line) divided by the Gaussian PSF.

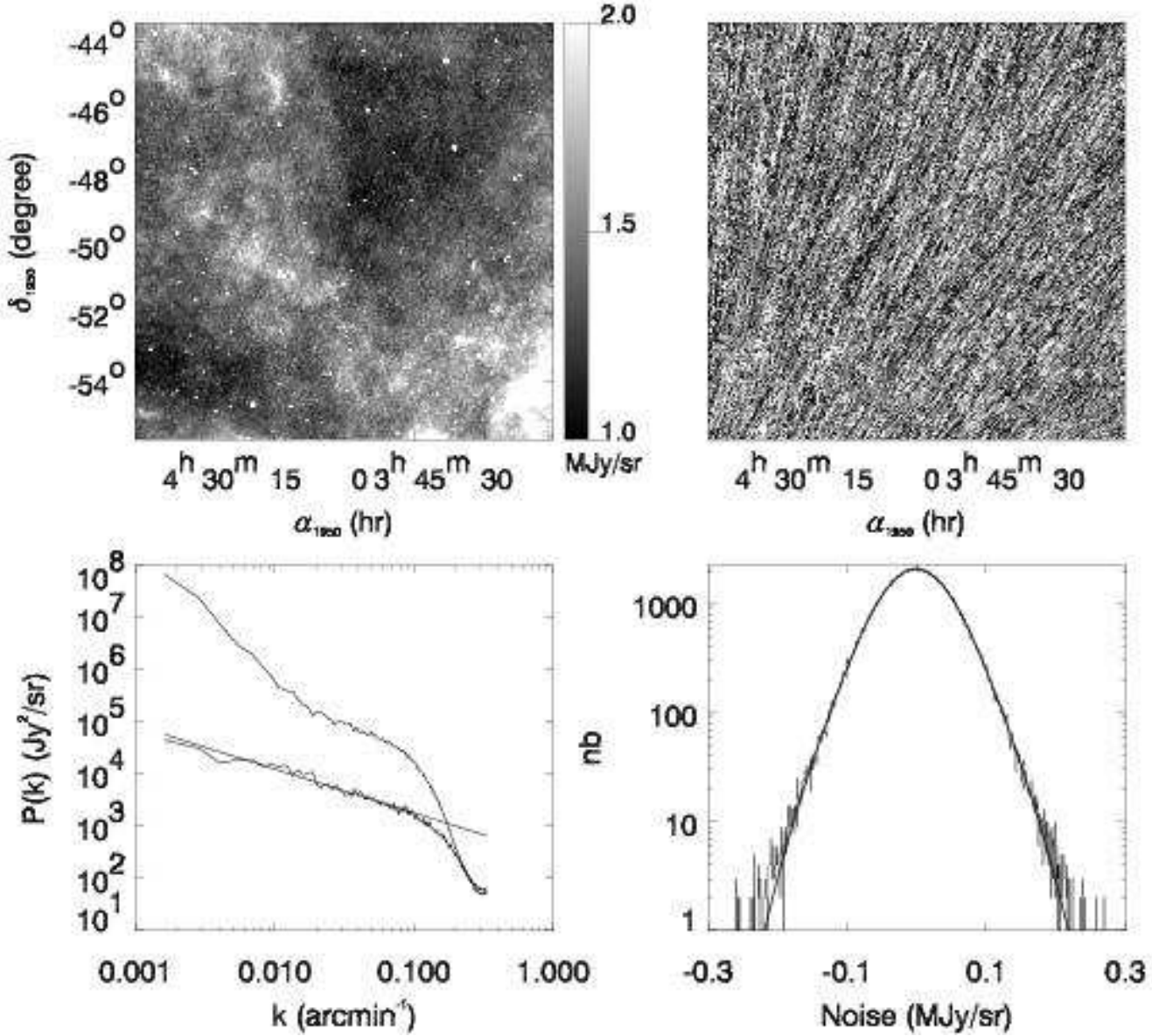


**Fig. 1.** **Top left:** The 100  $\mu\text{m}$  ISSA map number 47. **Top right:** Noise map of the 100  $\mu\text{m}$  map on the left. This noise map has been obtained by subtracting two individual HCON images that were used to build the ISSA map (see text for details). **Bottom left:** Power spectrum of the ISSA map (upper curve) and of the noise map. The power spectrum of the noise map has been fitted by a power law  $\propto k^{-0.83}$  for scales  $k \leq 0.1$  arcmin<sup>-1</sup>. Above  $k=0.1$  arcmin<sup>-1</sup>, the drop of the power spectrum is due to the instrumental function (see § 3.3). **Bottom right:** Histogram of the noise values, fitted by a sum of two Gaussian functions (Amplitude<sub>1</sub> = 1376,  $\sigma_1$  = 0.04 MJy/sr; Amplitude<sub>2</sub> = 711,  $\sigma_2$  = 0.06 MJy/sr).

### 3.3. Point spread function

The multiplicative factor  $\gamma(k)$  in Eq. 1 represents the effective instrumental filter function of the system (telescope, focal plane assembly, sky scanning and map making). For some ISSA maps the instrumental function can be estimated directly from the power spectrum of the map. This is the case for maps where the brightness fluctuations are dominated by the cirrus emission and where the power spectrum is simply:

$$P(k) = \gamma(k) \times P_{\text{dust}}(k). \quad (5)$$

Following Gautier et al. (1992), the power spectrum of the cirrus dust emission follows a power law ( $P_{\text{dust}}(k) = Ak^\beta$ ). This behavior has been confirmed through a detailed study of H I 21 cm emission by Miville-Deschênes et al. (2002). These studies show that although the power spectrum slope may vary from region to region by  $\sim 20\%$  there is no systematic break at high spatial frequencies. On the basis of these studies, we thus conclude that the power law representation for the cirrus power spectrum does not introduce any systematic effect.

To estimate  $\gamma(k)$  directly on the power spectrum of ISSA maps, we have selected 20 relatively bright regions (mean brightness greater than 8 MJy/sr) where the noise and CIB contributions are negligible. To make sure that the fluctuations are dominated by the cirrus emission, point sources were filtered out using a median filtering. An example of the power spectrum of such an ISSA map is shown in Fig. 2. We found that the effective IRAS instrumental filter function in Fourier space is well describe by a Gaussian function both at 60 and 100  $\mu\text{m}$ . To determine the width of the instrumental function, the power spectrum of the 20 fields were fitted by the following equation:

$$P(k) = \exp\left(\frac{-k^2}{2\sigma_k^2}\right) \times Ak^\beta \quad (6)$$

which represents the cirrus power law multiplied by the Gaussian instrumental function. We have found  $\sigma_k = 0.073 \pm 0.005$  at 60  $\mu\text{m}$  and  $\sigma_k = 0.065 \pm 0.005$  at 100  $\mu\text{m}$ . In the real space, this corresponds to a Gaussian instrumental function of  $\sigma = 1.5 \pm 0.1$  arcmin at 60  $\mu\text{m}$  and  $\sigma = 1.7 \pm 0.1$  arcmin at 100  $\mu\text{m}$ .<sup>1</sup>

The cutoff seen in Fig. 2 at frequencies larger than  $0.05 \text{ arcmin}^{-1}$  is where the effect of the instrumental filter function is expected. When the power spectrum is divided by the Gaussian instrumental function (grey line) one sees that this modeling does not stand for scales smaller than 4.5 arcminutes ( $k > 0.22 \text{ arcmin}^{-1}$ ). This is due to the effective resolution of the IRAS data. The power spectrum has to be cut at the Nyquist frequency corresponding to the 1.5' pixel ISSA map. However, the effective resolution of the IRAS data is about 3.8' and 4.25' respectively at 60 and 100  $\mu\text{m}$ . For that reason, all the power spectrum at frequency above  $0.1 \text{ arcmin}^{-1}$ , which corresponds to the Nyquist frequency of the effective resolution, has to be taken with cautious.

#### 4. Separation of the Galactic and extra-Galactic components

In Figs. A.2 to A.3 we present the power spectrum of the 60 and 100  $\mu\text{m}$  ISSA maps of our twelve fields (black line). For all these fields, the power spectrum of the noise has been subtracted and the result has been divided by the PSF  $\gamma(k)$ . At large scale, all the power spectra follow a power law typical of cirrus emission (Gautier et al. 1992). But at  $k \sim 0.01 \text{ arcmin}^{-1}$  we notice a break in the spectra and an excess from the cirrus power law at small scales. This power excess is observed for all our fields, at 60 and 100  $\mu\text{m}$ .

##### 4.1. Contribution of strong point sources

The power excess observed at small scales reveals the presence of a component with a flatter power spectrum,

<sup>1</sup> This is compatible with what we found by fitting a Gaussian function on point sources.

like what would be expected from noise or randomly distributed point sources. On the one hand, at this stage, a noise contribution is unlikely as it has been well estimated and removed accordingly. On the other hand, in fields with such low cirrus emission, several extra-galactic point sources were detected. In each of our fields, between 200 and 300 point sources are listed in the IRAS Point Source Catalog (PSC), the vast majority of them being extra-galactic objects. We remove the contribution of all point sources with flux greater than 1 Jy at 100  $\mu\text{m}$  (and the same sources at 60  $\mu\text{m}$ ). The cut at 1 Jy is chosen such that the PSC above this limit will be nearly complete. This gives a well define separation between the sources contributing to the unresolved CIB and the resolved sources. This is necessary for any quantitative use of our results. We choose this cut in flux as low as possible to remove the contribution of the nearby and resolved galaxies that dominate the power spectrum at scales  $k > 0.01 \text{ arcmin}^{-1}$  (for those galaxies, the spatial distribution is indistinguishable from a Poissonian distribution). Moreover, according to recent simulations, the cut of 1 Jy at 100  $\mu\text{m}$  almost corresponds to the flux where the non-euclidean part appears in the number counts. To remove the contribution of strong point sources ( $I_{100\mu\text{m}} \geq 1 \text{ Jy}$ ) to the power spectrum, they were filtered out from the ISSA map. For each ISSA map, we have extracted the point sources of the IRAS Point Source Catalog with a flux greater or equal to 1 Jy. Then we have applied a median filtering to the ISSA map to estimate the background level and, at each point source position, we have removed the points in a  $12 \times 12$  window that were more than 4 times the noise level ( $\sigma_{\text{issa}}$ ) above the background. Finally, the missing points were replaced by a bilinear interpolation.

The power spectrum of the filtered ISSA maps is the blue line in Figs A.2 to A.3. A power excess at small scales ( $k > 0.02 \text{ arcmin}^{-1}$ ) is still apparent on all power spectra, at 60 and 100  $\mu\text{m}$ . This excess is likely to be the signature of the unresolved cosmic far-infrared background. To characterize it, the contribution of the cirrus emission has to be removed.

##### 4.2. Contribution of the cirrus emission

As we do not have any independent tracers of the cirrus emission at the IRAS scales for the whole fields, the only way to derive the cirrus contribution is to use the statistical properties of their spatial distribution. Following Gautier et al. (1992) and Miville-Deschênes et al. (2002) the power spectrum of interstellar dust emission is well describe by a power law. To remove this contribution to the power spectrum of the filtered ISSA maps, we have fitted a power law on the large scale part of the power spectrum of the filtered maps. The best compromise between the number of point on which to fit the power law and the contamination from the CIB was to fit on  $k < 0.02 \text{ arcmin}^{-1}$ . The point corresponding to the largest scale was not used for the fitting as it suffers from a large sta-

tistical error. The result of the fitting, and its associated uncertainty, are shown for each ISSA map in Figs A.2 to A.3. The uncertainty on the slope reflects the dispersion of the points around the fit. The red line in these figures is the result of the subtraction of the cirrus power law from the power spectrum of the filtered map (blue line); it is the signature of the CIB.

#### 4.3. Contribution of the cosmic far-infrared background

The average of the 12 CIB contributions is shown in Fig. 3 (black lines). The blue lines in this figure indicate the  $1\sigma$  uncertainty on the determination, including the PSF and the estimate of the cirrus contribution errors. The  $1\sigma$  uncertainty is very close to the rms variations of the 12 averaged values. The dispersion between the fields is thus dominated by the PSF and cirrus contribution errors, we do not see any significant variation from field to field. Moreover, it is important to note that the detected excess at small scales is uncorrelated with the cirrus emission (the excess disappears when the cirrus contribution increases). Therefore, our fields being spread over the sky, the excess at small scale is compatible with isotropic properties. This is an other argument in favor of an extra-galactic origin for the excess.

We can note on Fig. A.2-9 that the power spectrum of the resolved IRAS sources is varying by factor up to 10 from field to field. The CIB (resolved and unresolved) fluctuations are dominated by the brightest sources in ISSA maps. The number of such sources is quite small, leading to a high cosmic variance, and thus large variation from field to field. On the contrary, for the unresolved CIB fluctuations, as sources above 1 Jy (about 300 per field) are removed, the cosmic variance is lower than 6%, which is negligible with respect to the  $1\sigma$  uncertainty.

The CIB is detected over one decade in scales, from 5 to 50 arcminutes. The power spectrum of the CIB at 60 and 100  $\mu\text{m}$  is compatible with a Poissonian distribution at spatial frequencies between 0.025 and 0.2 arcmin $^{-1}$ . The fluctuation level is  $\sim 1.6 \times 10^3 \text{ Jy}^2/\text{sr}$  and  $\sim 5.8 \times 10^3 \text{ Jy}^2/\text{sr}$  at 60 and 100  $\mu\text{m}$  respectively.

## 5. Discussion

### 5.1. CIB fluctuations at 60 and 100 $\mu\text{m}$

We have shown here that the power spectrum of high latitude fields at 60 and 100  $\mu\text{m}$  is characterized by a break at small scales (near 0.02 arcmin $^{-1}$ ). As indicated by Gautier et al. (1992), the power spectrum of the dust emission is usually well described by a power law proportional to  $k^{-3 \pm 0.2}$ . A more detailed study of the statistical properties of the interstellar cirrus HI 21 cm emission has been carried out by Miville-Deschênes (1999). In this analysis it is shown that there are limited variations of the spectral index of the power law from field to field but, what is most important for the present work, the power spec-

trum of cirrus emission for scales smaller than 12.5 $^\circ$  is always characterized by a single power law with no break. Therefore, it is unlikely that the power excess observed here at small scales is of interstellar origin.

We could also wonder if this break is of instrumental origin. It was shown by Wheelock et al. (1993) that the response of the IRAS detectors are affected by memory effects. This produces variations of the detector response as a function of scale. This effect is more important at small scales (under a few tens of arcminutes) but Wheelock et al. (1993) have shown that the amplitude of the fluctuations at these scales were underestimated. This effect will thus produce a drop of the power spectrum at small scale and cannot explain the power excess observed here.

On the other hand, instrumental noise could produce such an excess in the power spectrum. But, as the IRAS ISSA maps result from redundant individual observations, we were able to estimate the contribution of the noise to the power spectrum. We are aware that our estimate of the noise rely on the fact that the individual HCONs are independant. This is not perfectly true as, in the construction of the HCONs, an offset was added to each scan to minimize the difference between different observations of the same position. Therefore the noise level estimated by subtracting HCONs may be underestimated at the scale of a scan, which is a few degrees. But at this angular scale the signal is completely dominated by the cirrus emission, even in the low brightness regions selected for our analysis. At the scale of a few arcminutes where the CIB is detected, the noise contribution to the power spectrum has been removed accurately.

In fact it appears that most of the power excess can be attributed to the numerous extra-galactic point sources that are present in such a low cirrus emission field. When the strong ( $I_{100\mu\text{m}} > 1 \text{ Jy}$ ) point sources are removed from the ISSA maps, we recover a power spectrum typical of cirrus emission at low spatial frequencies but with still a power excess at small scales ( $k > 0.02 \text{ arcmin}^{-1}$ ) that can be attributed to the unresolved cosmic infrared background. Moreover, the residue has homogeneous properties over the sky, consistent with CIB.

Knox et al. (2001) computed the expected power spectrum of the CIB at several frequencies ( $\nu \leq 1060 \text{ GHz}$ ), exploiting the far-IR volume emissivity derived from the count models of Guiderdoni et al. (1998) and assuming a bias  $b = 3$ , constant with redshift. They concluded that the clustering-induced fluctuations can match those of the CMB at  $\ell \lesssim 300$ . They also predict a shape of the CIB power spectrum peaking around scales of 1-3 degrees. This broad maximum, if present, is at the limit of our frequency range where the noise is becoming large, making the detection of the clustering very difficult. The power spectra of the CIB at 60 and 100  $\mu\text{m}$  are compatible with a Poissonian distribution with levels  $\sim 1.6 \times 10^3 \text{ Jy}^2/\text{sr}$  and  $\sim 5.8 \times 10^3 \text{ Jy}^2/\text{sr}$  respectively.

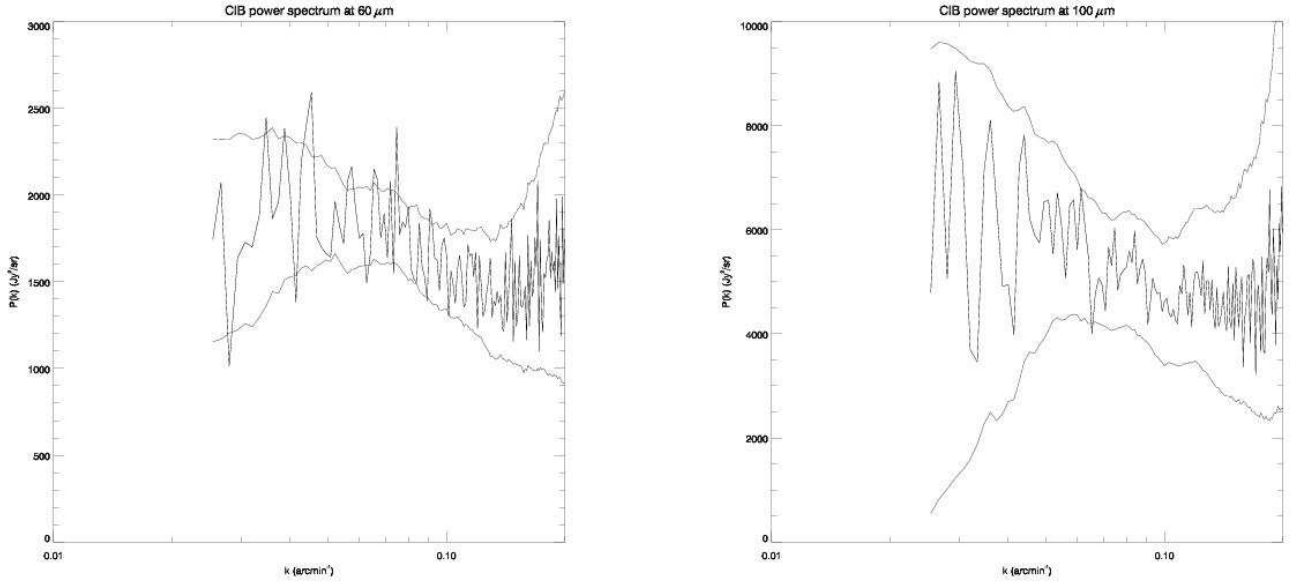


**Fig. 3.** CIB contributions to the 60 (left) and 100  $\mu\text{m}$  (right) power spectra. The black line is the average of the CIB contributions for the 12 fields. The blue lines indicates the uncertainty on the CIB contribution, computed from the uncertainty on the cirrus slope and on the PSF width.

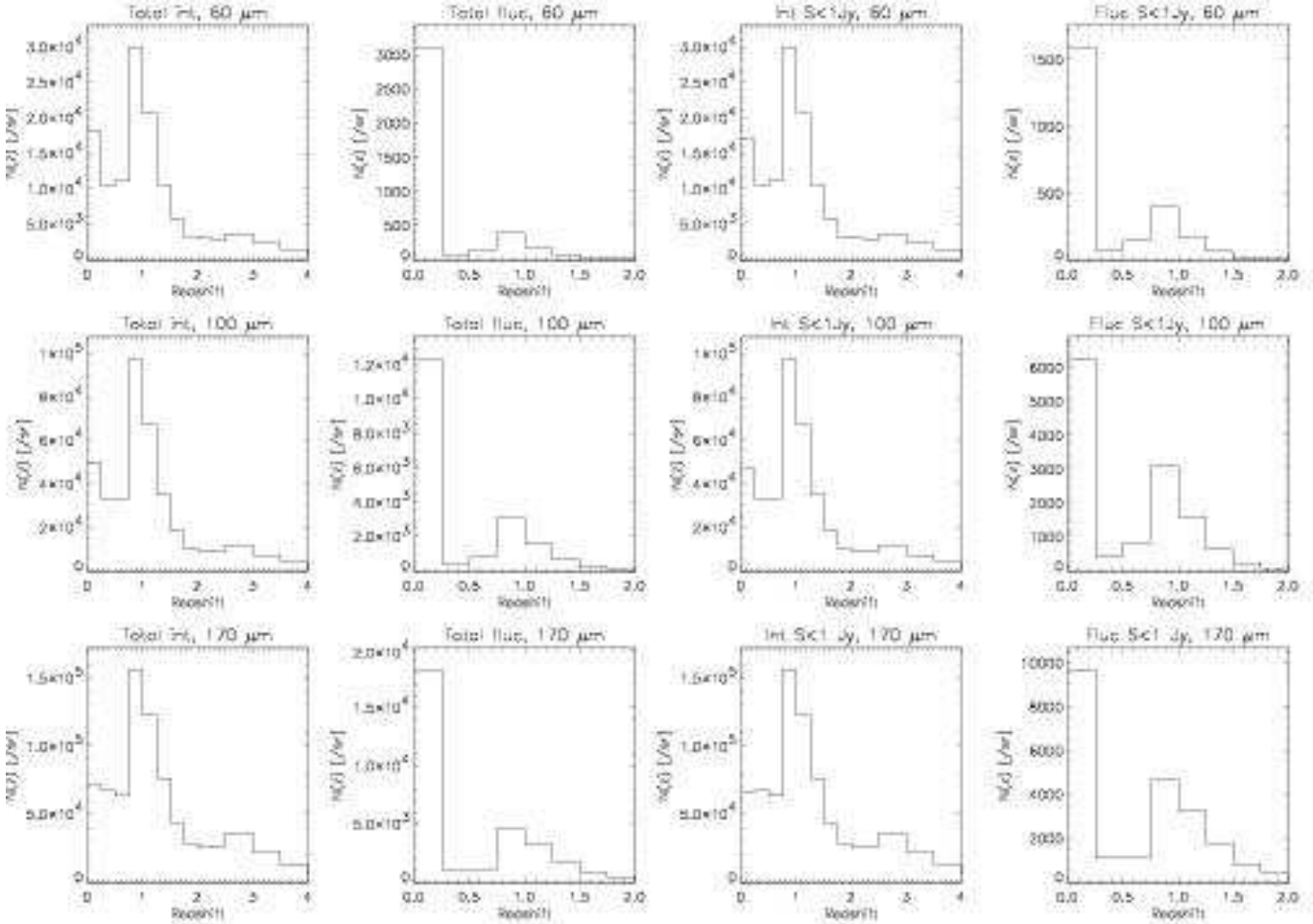


**Fig. 4.** Redshift distribution of the sources making the CIB and the fluctuations at 60, 100 and 170  $\mu\text{m}$ . The first two-left panels are for the total contributions, the last two-right panels, for sources with flux below 1 Jy (Lagache et al. 2002)

### 5.2. CIB intensity and anisotropy amplitudes color ratio

The CIB rms fluctuations in the IRAS maps corresponding to the white noise power spectra are:

$$\sigma^2 = \int P_{\text{cib}}(k) 2\pi k dk \quad \text{Jy}^2/\text{sr}^2 \quad (7)$$

giving  $\sigma=0.048$  MJy/sr and  $\sigma=0.09$  MJy/sr at 60 and 100  $\mu\text{m}$  respectively. As shown by Gispert et al. (2000), the CIB at different wavelengths is dominated by sources at different redshifts, larger wavelengths being dominated by more distant sources. The same applies to the fluctuations: lower frequencies probe higher redshifts (e.g. Knox et al. (2001)) The fluctuations at 60  $\mu\text{m}$  are dominated by nearby bright objects. When we remove these objects, the residual fluctuations are quite low. At 100  $\mu\text{m}$ , the contribution of higher redshift objects is increasing, leading to higher level of residual fluctuations. Therefore, the ratio of the 60 to 100  $\mu\text{m}$  fluctuation is qualitatively consistent with what is expected.

This is illustrated more quantitatively in Fig.4 on the panels showing the redshift distribution of sources contributing to the CIB intensity and the fluctuations (Lagache et al. 2002). It is clear from these figures that the z-distribution of the fluctuations is bimodal, with one contribution at redshift lower than 0.25 and the other one centered at redshift around 1. For all sources the ratio of nearby to moderate-redshift source contribution to the fluctuations is equal to 3.8, 1.8 and 1.3 at 60, 100, 170  $\mu\text{m}$  respectively, illustrating that fluctuations at larger wavelengths are dominated by more distant sources. When the brightest sources are removed the ratio of nearby to moderate-redshift contribution becomes equal to 1.7, 1 and 0.74 at 60, 100, 170  $\mu\text{m}$ . In this case, at 100  $\mu\text{m}$  the contribution to the fluctuations of nearby and moderate-redshift sources is the same, becoming lower at higher wavelength. At 60  $\mu\text{m}$ , the fluctuations are still dominated by the nearby objects.

For the three wavelengths, the CIB is mainly due to sources at redshift around 1. A detailed analysis of the CIB fluctuations at 100 and 170  $\mu\text{m}$  (which is beyond the scope of this paper) will give information on the distribution of sources at  $z \sim 1$  making the bulk of the CIB. This is particularly true at 170  $\mu\text{m}$  where sources with flux lower than  $4\sigma=135$  mJy can be removed (Dole et al. 2001), leading fluctuations highly dominated by the moderate-z sources.

We can compute the ratio of CIB fluctuations to intensity ( $R_\lambda = \frac{\sigma_\lambda}{I_\lambda}$ ) at 100  $\mu\text{m}$  and compare it with the previous determination at 170  $\mu\text{m}$ . To compute  $R_{100}$  and  $R_{170}$ , we use:

- a CIB intensity at 100  $\mu\text{m}$  of 0.5 MJy/sr (Renault et al. 2001), leading to  $R_{100} = 0.18$
- a CIB intensity at 170  $\mu\text{m}$  of 1 MJy/sr Lagache & Dole (2001). For the fluctuations, we assume that a cut of 1 Jy at 60 and 100  $\mu\text{m}$  corresponds to the same cut at 170  $\mu\text{m}$ . We obtain rms fluctuations of 0.12 MJy/sr

(corresponding to  $\sim 11000$  Jy<sup>2</sup>/sr, (Puget & Lagache 2002)). This gives  $R_{170} = 0.12$

The ratio R is decreasing between 100 and 170  $\mu\text{m}$ , as expected. At 60  $\mu\text{m}$ , the minimal hypothesis is to consider that  $R_{60}$  is equal to  $R_{100}=0.18$  which gives an upper limit of 0.27 MJy/sr on the CIB intensity. An illustrative logarithmic extrapolation of R out to 60  $\mu\text{m}$  gives  $R_{60}=0.27$  leading to an estimate of the CIB intensity at 60  $\mu\text{m}$  of 0.18 MJy/sr, which is significantly smaller than the previous determination of Finkbeiner et al. (2000) of 0.56 MJy/sr.

### 5.3. Implication for the component separation

This work suggests that the high latitude IRAS maps, in the lowest cirrus regions, cannot be used as a tracer of the interstellar extinction structure as proposed by (Schlegel et al. 1998). In fact it should be noted that it is only above an intensity of order of 10 MJy/sr at 100  $\mu\text{m}$  that the CIB fluctuations are lower than the cirrus contribution at the smallest scales ( $k \sim 0.2$  arcmin<sup>-1</sup>).

Present and future CMB observations, above 100 GHz, with high sensitivity bolometers need to remove foreground contributions (cirrus and CIB fluctuations). The CIB spectrum being significantly “colder” than the cirrus spectrum ( $I_{\text{cirrus}100\mu\text{m}}/I_{\text{cirrus}1\text{mm}} \sim 30$ ;  $I_{\text{CIB}100\mu\text{m}}/I_{\text{CIB}1\text{mm}} \sim 5$ ), the relative contribution of the CIB will increase with wavelength. It is thus expected that at 1 mm the range in l space dominated by the CIB will be much more extended than seen at 100  $\mu\text{m}$ . This question will be dealt in a forthcoming paper.

### Acknowledgements

*The Fond FCAR du Québec provided funds to support this research project.*

### References

- Dole, H., Gispert, R., Lagache, G., et al., 2001, A&A, 372, 364.
- Dwek, E., Arendt, R. G., Hauser, M. G., et al., 1998, ApJ, 508, 106.
- Finkbeiner, D. P., Davis, M. & Schlegel, D. J. 2000, ApJ, 544, 81.
- Gautier, T. N. I., Boulanger, F., Perault, M. & Puget, J. L. 1992, AJ, 103, 1313.
- Gispert, R., Lagache, G. & Puget, J. L. 2000, A&A, 360, 1.
- Guiderdoni, B., Hivon, E., Bouchet, F. R. & Maffei, B. 1998, MNRAS, 295, 877.
- Hauser, M. G. & Dwek, E. 2001, ARA&A, 39, 249.
- Knox, L., Cooray, A., Eisenstein, D. & Haiman, Z. 2001, ApJ, 550, 7.
- Lagache, G. & Dole, H. 2001, A&A, 372, 702.
- Lagache, G. & Puget, J. L. 2000, A&A, 355, 17.
- Lagache, G., Dole, H. & Puget, J. L. submitted to MNRAS, 2002.



- Marano, B., Zamorani, G. & Zitelli, V. 1988, MNRAS, 232, 111.
- Matsuhara, H., Kawara, K., Sato, Y., et al., 2000, A&A, 361, 407.
- Miville-Deschênes, M. A., Joncas, G., Flagarone, E. & Boulanger, F. in preparation, 2002.
- Miville-Deschênes, M. A. PhD thesis, Université Paris XI (France) and Université Laval (Québec), 1999.
- Peacock, J. A., Rowan-Robinson, M., Blain, A. W., et al., 2000, MNRAS, 318, 535.
- Puget, J. L. & Lagache, G. In *The extragalactic infrared background and its cosmological implication*. IAU, symposium 204, 2002.
- Puget, J. L., Abergel, A., Bernard, J. P., et al., 1996, A&A, 308, L5.
- Renault, C., Barrau, A., Lagache, G. & Puget, J. L. 2001, A&A, 371, 771.
- Schlegel, D. J., Finkbeiner, D. P. & Davis, M. 1998, ApJ, 500, 525.
- Wheelock, S., Gautier, T. N., Chillemi, J., et al., Issa explanatory supplement. Technical report, Infrared Processing and Analysis Center, 1993.

## Appendix A: Power spectrum computation method

The power spectrum of an image  $f(x, y)$  of Fourier Transform  $\tilde{f}(k_x, k_y)$  is computed from the amplitude  $A(k_x, k_y)$  defined as

$$A(k_x, k_y) = \tilde{f}(k_x, k_y) \tilde{f}^*(k_x, k_y) = |\tilde{f}(k_x, k_y)|^2. \quad (\text{A.1})$$

The power spectrum  $P(k)$  is the average of  $A(k_x, k_y)$  on annulus of constant  $k = \sqrt{k_x^2 + k_y^2}$ . The amplitude image of a typical ISSA map is shown in Fig A.1 (top-right). In this figure, the frequency  $k = 0$  is at the center of the amplitude image. The amplitude decreases with increasing value of  $k$  but one also notices the presence of a cross that reveals an increase of the fluctuation level in the horizontal and vertical directions. This cross is caused by the Fast Fourier Transform algorithm that makes an “infinite pavement” with the image prior to compute the Fourier Transform. As the ISSA images are not periodic objects, this operation produces discontinuities where the left (top) meets the right (bottom) side of the image. These horizontal and vertical discontinuities are responsible for the cross seen in the amplitude image. The main problem with this cross is that it increases artificially the power when the average over  $k$  is done. Furthermore, the power increase is not constant as a function of  $k$  which modify the slope of the spectrum as well as the normalization.

The usual method to get rid of this effect is to apodize the image so that the left (top) and right (bottom) sides of the image have a similar flux level. Another method which does not modify the image but acts on the amplitude image itself is to compute  $P(k)$  by taking the *median* value at constant  $k$ . For  $\sim 85\%$  of the ISSA maps we have inspected, these two methods give very similar results. But when the cross is very strong, the power at small scales is still overestimated by the “median” method. Furthermore, at small  $k$  values, there are less points to average and a large fraction of them are affected by the cross effect; at these frequencies, the median value may not be significant. For all these reasons, we have adopted the “apodization” method.

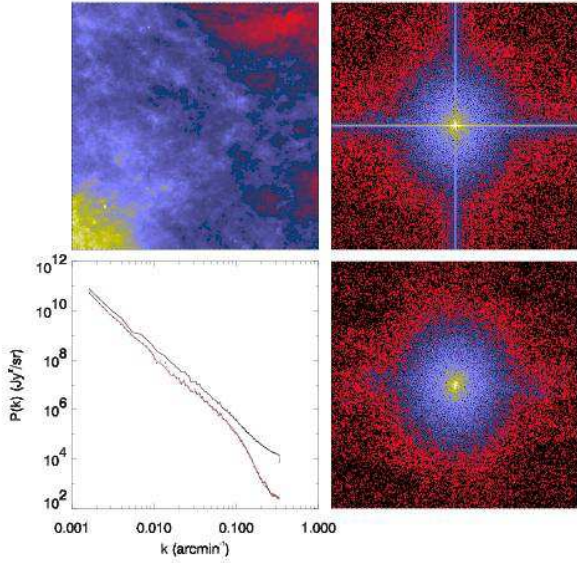


**Fig. A.1.** **Upper left:** Typical ISSA map with a large scale gradient. **Upper right:** Amplitude of the Fourier Transform of the image on the left. The cross seen here is produced by the left-right and top-bottom flux difference in the image. **Lower right:** Amplitude of the Fourier Transform of the image apodized with a cosine function to minimize the left-right and top-bottom discontinuities. **Lower left:** Power spectrum of the original image (solid line) and of the apodized image (red line). The power spectrum computed with the Median method is also shown (dotted line). It follows almost perfectly the power spectrum of the apodized image.

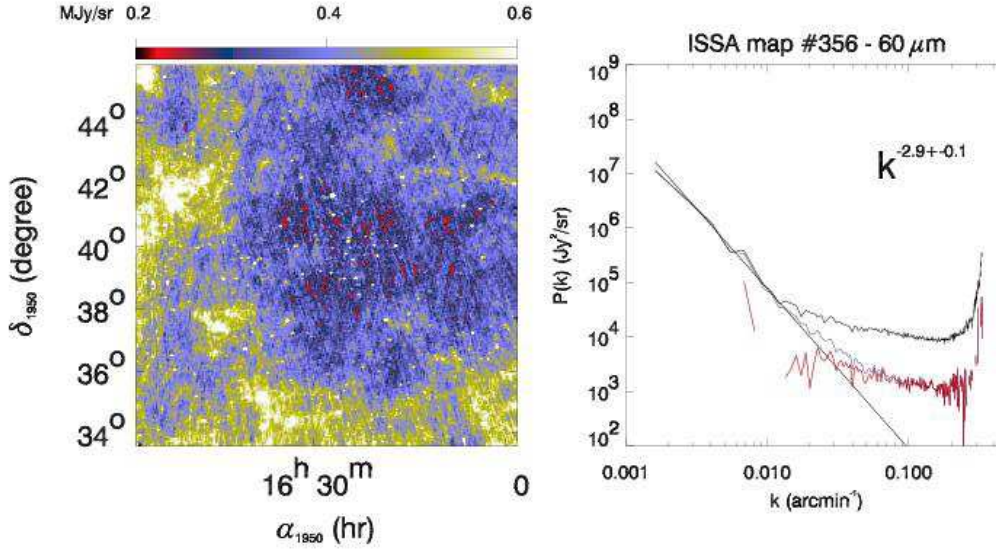


**Fig. A.2.** Power spectrum of a typical 60  $\mu\text{m}$  ISSA maps. The black curve is the power spectrum of the raw ISSA map from which the power spectrum of the noise has been subtracted. The blue curve is the power spectrum (also noise subtracted) of the map from which point sources stronger than 1 Jy in the IRAS point sources catalog were removed. A power law fit of the blue curve (for  $k < 0.02 \text{ arcmin}^{-1}$ ) is also shown. The red curve is the difference between the blue curve and the power law fit.

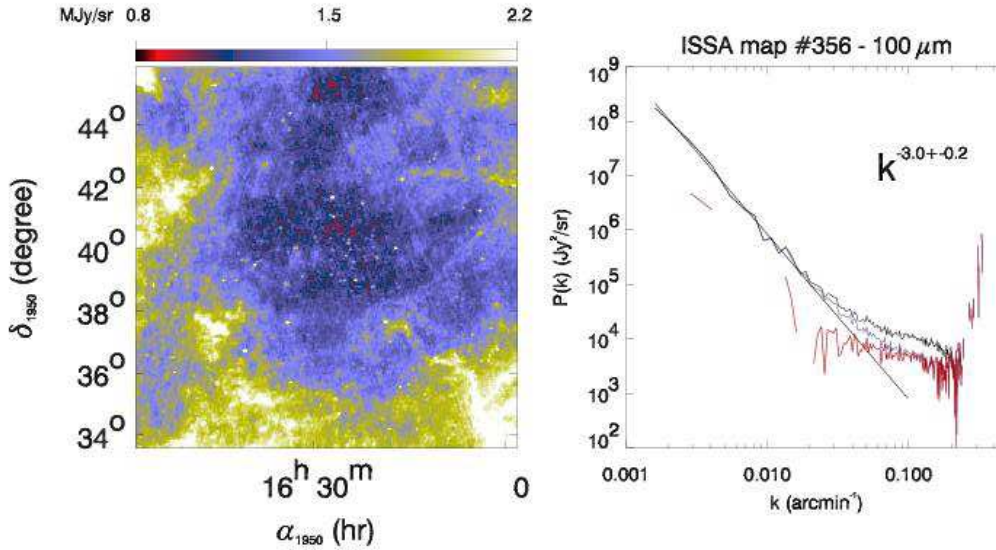


**Fig. A.3.** Power spectrum of a typical 100  $\mu\text{m}$  ISSA maps. The black curve is the power spectrum of the raw ISSA map from which the power spectrum of the noise has been subtracted. The blue curve is the power spectrum (also noise subtracted) of the map from which point sources stronger than 1 Jy in the IRAS point sources catalog were removed. A power law fit of the blue curve (for  $k < 0.02 \text{ arcmin}^{-1}$ ) is also shown. The red curve is the difference between the blue curve and the power law fit.